CP violation and determination of the *bs* flat unitarity triangle at an FCC-ee

R. Aleksan,[1] L. Oliver,[2] and E. Perez[3]

[1]*IRFU, CEA, Université Paris-Saclay, 91191 Gif-sur-Yvette cedex, France*
[2]*IJCLab, Pôle Théorie, CNRS/IN2P3 et Université Paris-Saclay, bât. 210, 91405 Orsay, France*
[3]*CERN, EP Department, Geneva, Switzerland*

(Received 10 December 2021; accepted 28 January 2022; published 25 March 2022)

We investigate the sensitivity with which two angles of the flat unitarity triangle, defined by $V_{ub}^* V_{us} + V_{cb}^* V_{cs} + V_{tb}^* V_{ts} = 0$, can possibly be measured directly at FCC-ee. We show that the measured errors on the angle $\alpha_s = \arg(-V_{ub}^* V_{us}/V_{tb}^* V_{ts})$ and $\beta_s = \arg(-V_{tb}^* V_{ts}/V_{cb}^* V_{cs})$ should be better than 0.4° and 0.035°, respectively. These measurements, combined with the measurement of the third angle $\gamma_s = \arg(-V_{cb}^* V_{cs}/V_{ub}^* V_{us})$, discussed in a different paper, will contribute to probing the consistency of the *CP* sector of the Standard Model further with an unprecedented level of accuracy.

DOI: 10.1103/PhysRevD.105.053008

I. INTRODUCTION

The purpose of this paper is to study with what accuracy can the angles of a "nonusual" unitarity triangle be determined directly at the FCC-ee. Indeed, in most of the publications, the authors concentrate on the "so called" unitarity triangle, one of whose angles is obtained from the "golden" channel $B^0(\bar{B}^0) \to J/\psi K_s$. This triangle has its three sides of the same order of magnitude and is therefore the less difficult to measure. However, there are five other triangles, two of which are rather flat, and the other two are very flat. In order to test the Standard Model (SM) more thoroughly, it would be interesting to measure these other triangles directly and independently. By *directly* we mean the measurement of an angle without making use of its relations to other angles in the SM. In this paper we investigate the sensitivity which one may expect at FCC-ee [1–3].

In the SM, one derives the unitarity relations from the CKM quark mixing matrix [4],

$$V_{\rm CKM} = \begin{bmatrix} V_{ud} & V_{us} & V_{ub} \\ V_{cd} & V_{cs} & V_{cb} \\ V_{td} & V_{ts} & V_{tb} \end{bmatrix} \tag{1}$$

If there are only three families of quarks, the unitarity relations, which are derived from $V_{\rm CKM} V_{\rm CKM}^\dagger = 1$, read as

$$\begin{aligned} UT_{db} &\equiv V_{ub}^* V_{ud} + V_{cb}^* V_{cd} + V_{tb}^* V_{td} = 0 \\ UT_{sb} &\equiv V_{ub}^* V_{us} + V_{cb}^* V_{cs} + V_{tb}^* V_{ts} = 0 \\ UT_{ds} &\equiv V_{us}^* V_{ud} + V_{cs}^* V_{cd} + V_{ts}^* V_{td} = 0 \end{aligned} \tag{2}$$

plus three additional triangular relations. The three relations of Eq. (2) are visualized in Fig. 1.

In the SM, the CKM matrix has only four independent parameters. Therefore the angles of these triangles can be expressed in terms of four angles [5]. The first relation in Eq. (2) is known as the unitarity triangle, with the three sides of the same order, and has been studied extensively.

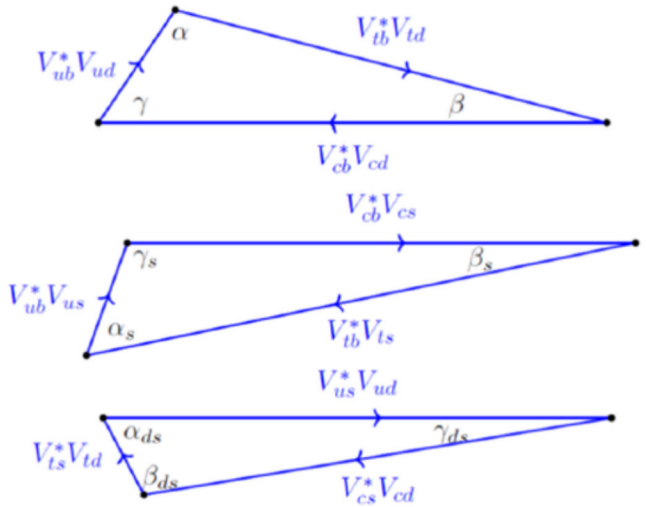

FIG. 1. Unitarity triangle UT_{db} involving the first and third columns (top), Unitarity Triangle UT_{sb} involving the second and third columns (center) and Unitarity Triangle UT_{ds} involving the first and second columns (bottom) of the CKM matrix. Note that these triangles are not to scale.

However the other ones deserve to be studied in detail as well, in order to investigate the consistency of the SM further.

We define the angles of these triangles as

$$\alpha = \arg\left(-\frac{V_{tb}^* V_{td}}{V_{ub}^* V_{ud}}\right), \qquad \beta = \arg\left(-\frac{V_{cb}^* V_{cd}}{V_{tb}^* V_{td}}\right),$$
$$\gamma = \arg\left(-\frac{V_{ub}^* V_{ud}}{V_{cb}^* V_{cd}}\right), \tag{3}$$

$$\alpha_s = \arg\left(-\frac{V_{ub}^* V_{us}}{V_{tb}^* V_{ts}}\right), \qquad \beta_s = \arg\left(-\frac{V_{tb}^* V_{ts}}{V_{cb}^* V_{cs}}\right),$$
$$\gamma_s = \arg\left(-\frac{V_{cb}^* V_{cs}}{V_{ub}^* V_{us}}\right), \tag{4}$$

$$\alpha_{ds} = \arg\left(-\frac{V_{us}^* V_{ud}}{V_{ts}^* V_{td}}\right), \qquad \beta_{ds} = \arg\left(-\frac{V_{ts}^* V_{td}}{V_{cs}^* V_{cd}}\right),$$
$$\gamma_{ds} = \arg\left(-\frac{V_{cs}^* V_{cd}}{V_{us}^* V_{ud}}\right), \tag{5}$$

For the angles α, β, and γ of the triangle UT_{db} we have adopted the usual convention with circular permutation of the quarks t, c, u. For the triangle UT_{sb}, we have adopted the generally accepted notation for β_s [6], and for the other angles the corresponding circular permutations of t, c, u. For the triangle UT_{ds}, we have used the notation of UT_{sb} with the replacement $b \to s, s \to d$.

To get a feeling on how these different triangles compare in the CKM scheme, let us give the angles of UT_{sb} and UT_{sd} using the Particle Data Group (2020) improved Wolfenstein parametrization with the central values for the relevant parameters $\lambda \simeq 0.226, A \simeq 0.790, \eta \simeq 0.357, \rho \simeq 0.141$ [7], that fit the ordinary unitarity triangle UT_{db},

$$UT_{sb}\colon\ (\alpha_s, \beta_s, \gamma_s) \simeq (1.177, 0.018, 1.947),$$
$$UT_{ds}\colon\ (\alpha_{ds}, \beta_{ds}, \gamma_{ds}) \simeq (0.402, 2.748, 5.8 \times 10^{-4}). \tag{6}$$

In this paper we concentrate on the triangle UT_{sb}, which is rather "flat" since two of its sides are of order λ^2, where $\lambda = \sin\theta_c \simeq 0.22$, while the third side is of order λ^4. The three angles of this triangle can be measured directly at the FCC-ee. The angle β_s can be measured with precision through the well-known, and already widely used, final states $\bar{B}_s(B_s) \to J/\psi\phi$ or $J/\psi\eta$. Once this angle is known, one could measure the angle α_s by the final states $\bar{B}_s(B_s) \to D_s^+ K^-$, $D^0\phi$, and their CP conjugated modes $B_s(\bar{B}_s) \to D_s^- K^+$, $\bar{D}^0\phi$, as will be discussed below.

Finally, the decays $B^\pm \to \bar{D}^0(D^0)K^\pm$ (and their CP conjugates) can determine the angle γ_s, as will be discussed in a separate paper [8].

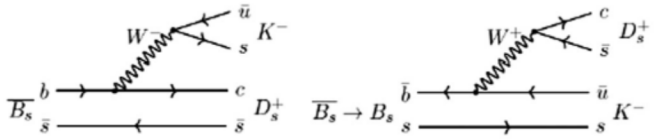

FIG. 2. The leading Feynman diagrams for the $\overline{B_s}$ decay to the final state $D_s^+ K^-$. There are also exchange diagrams, which are expected to be small and involve the same CKM elements.

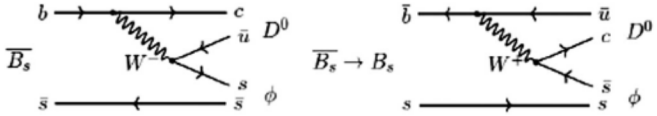

FIG. 3. The leading Feynman diagrams for the $\overline{B_s}$ decay for the final state $D^0\phi$. There are also exchange diagrams, which are expected to be small and involve the same CKM elements.

II. STUDY OF INTERFERENCE EFFECT FOR $\overline{B_s}(B_s)$ INDUCED THROUGH THE INTERPLAY OF MIXING AND DECAY

A. B_s decays to non-CP eigenstates

We first investigate the sensitivity for measuring CP violation at FCC-ee with the modes $\overline{B_s}(B_s) \to D_s^+ K^-, D^0\phi$ and their CP conjugates (see Figs. 2 and 3), that measure the same CP violating phase [9].

The eigenstates of the 2×2 B_s mass matrix $M - \frac{i}{2}\Gamma$ are written in terms of the B_s and $\overline{B_s}$ states as follows:

$$|B_{L(H)}\rangle = p|B_s\rangle + (-)q|\overline{B_s}\rangle, \tag{7}$$

In the Standard Model the box diagrams in Fig. 4, which are responsible for $B_s - \overline{B_s}$ mixing, dominated by t-quark exchange. Thus, one can safely use the approximation $|q/p| \simeq 1$, where q/p is given by a ratio of CKM matrix elements $V_{tb}^* V_{ts}$. This approximation is good at the sub per mille level,

$$\left(\frac{q}{p}\right)_{B_s} = -\sqrt{\frac{M_{12}^*}{M_{12}}} \simeq -\frac{V_{tb}^* V_{ts}}{V_{tb} V_{ts}^*}. \tag{8}$$

Similarly the phase of q/p is given by $\arg(-V_{tb}^* V_{ts}/V_{tb}V_{ts}^*)$ to a sub per mille level as well. Note that the quantity above is not invariant under phase convention and thus is not an observable. Let us now write also

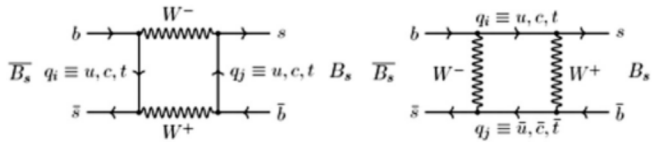

FIG. 4. The box Feyman diagrams for the $\overline{B_s} - B_s$ mixing, dominated by t-quark exchange in the SM.

$$\lambda(f)=\frac{q}{p}\frac{\langle f|\overline{B_s}\rangle}{\langle f|B_s\rangle},\qquad \bar{\lambda}(\bar{f})=\frac{p}{q}\frac{\langle \bar{f}|B_s\rangle}{\langle \bar{f}|\overline{B_s}\rangle},$$
$$\lambda(\bar{f})=\frac{q}{p}\frac{\langle \bar{f}|\overline{B_s}\rangle}{\langle \bar{f}|B_s\rangle},\qquad \bar{\lambda}(f)=\frac{p}{q}\frac{\langle f|B_s\rangle}{\langle f|\overline{B_s}\rangle},\tag{9}$$

and with the notation $\rho=|\lambda(f)|$, one has

$$\lambda(f)=\rho e^{i(\phi_{\rm CKM}+\delta_s)},\qquad \bar{\lambda}(\bar{f})=\rho e^{i(-\phi_{\rm CKM}+\delta_s)},$$
$$\lambda(\bar{f})=\frac{1}{\rho}e^{i(\phi_{\rm CKM}-\delta_s)},\qquad \bar{\lambda}(f)=\frac{1}{\rho}e^{-i(\phi_{\rm CKM}+\delta_s)},\tag{10}$$

where $\phi_{\rm CKM}$ and δ_s are the CKM phase difference and strong phase difference of the two diagrams in Fig. 2, respectively.

Some words of caution. Note that Eqs. (10) are relevant only for $\rho\neq 0$. It is indeed the case for the modes $\overline{B_s}(B_s)\to D_s^+K^-$ and their CP conjugates, as can be seen from the two diagrams of Fig. 2. However, for the pionic mode $\overline{B_s}\to D_s^+\pi^-$ and its *CP* conjugate, which are useful to measure the mixing parameter and wrong tagging fraction, as will be discussed below, it is not possible to get the same final state through $\overline{B_s}-B_s$ mixing, and only the decays $\langle\bar{f}|\overline{B_s}\rangle$ and $\langle f|B_s\rangle$ are possible. The complete time-dependent decay widths are

$$\Gamma(B_s(t)\to f)=|\langle f|B_s\rangle|^2e^{-\Gamma t}\left\{\frac{1+\rho^2}{2}\cosh\frac{\Delta\Gamma t}{2}+\frac{1-\rho^2}{2}\cos\Delta mt+\rho\cos\phi_{CP}^{+}\sinh\frac{\Delta\Gamma t}{2}-\rho\sin\phi_{CP}^{+}\sin\Delta mt\right\},$$
$$\Gamma(\overline{B_s}(t)\to f)=|\langle f|B_s\rangle|^2e^{-\Gamma t}\left\{\frac{1+\rho^2}{2}\cosh\frac{\Delta\Gamma t}{2}-\frac{1-\rho^2}{2}\cos\Delta mt+\rho\cos\phi_{CP}^{+}\sinh\frac{\Delta\Gamma t}{2}+\rho\sin\phi_{CP}^{+}\sin\Delta mt\right\},$$
$$\Gamma(B_s(t)\to \bar{f})=|\langle f|B_s\rangle|^2e^{-\Gamma t}\left\{\frac{1+\rho^2}{2}\cosh\frac{\Delta\Gamma t}{2}-\frac{1-\rho^2}{2}\cos\Delta mt+\rho\cos\phi_{CP}^{-}\sinh\frac{\Delta\Gamma t}{2}-\rho\sin\phi_{CP}^{-}\sin\Delta mt\right\},$$
$$\Gamma(\overline{B_s}(t)\to \bar{f})=|\langle f|B_s\rangle|^2e^{-\Gamma t}\left\{\frac{1+\rho^2}{2}\cosh\frac{\Delta\Gamma t}{2}+\frac{1-\rho^2}{2}\cos\Delta mt+\rho\cos\phi_{CP}^{-}\sinh\frac{\Delta\Gamma t}{2}+\rho\sin\phi_{CP}^{-}\sin\Delta mt\right\},\tag{11}$$

In Eq. (11), terms of order $a=\mathrm{Im}\frac{\Gamma_{12}}{m_{12}}$ have been neglected ($|q/p|^2=1-a$), $\rho=|\lambda(f)|$ is the modulus of the ratio of the amplitudes (10), $\Delta m=m_H-m_L\simeq 17.757\ \mathrm{ps}^{-1}$ is the mass difference between the B_s eigenstates (H, L stand for heavy and light states), $\Gamma=\frac{\Gamma_H+\Gamma_L}{2}$, $\Delta\Gamma=\Gamma_L-\Gamma_H$ (so that $\Delta\Gamma>0$ for K and B_s mesons), and $\phi_{CP}^{\pm}=\phi_{\rm CKM}\pm\delta_s$, where $\phi_{\rm CKM}$ is the *CP*-violating weak phase and δ_s is the difference between the strong phases of the interfering diagrams (see for example Fig. 2). Moreover, if the time dependence is normalized to an integrated finite interval in t that is not $[0,\infty]$, one should introduce a normalization factor N_f in (11).

In the following, for the sake of simplicity, we neglect the width difference $\Delta\Gamma_s=(0.090\pm0.005)\times10^{12}s^{-1}$ [7], the effect of which is negligible in this study. Note however that these terms with $\Delta\Gamma_s$ help to remove ambiguities for the extraction of $\phi_{\rm CKM}$.

In order to observe these distributions experimentally, one needs to tag the nature (B_s or $\bar{B}_s$) of the initial B-meson. Unfortunately, this tagging is imperfect, and one needs to introduce the wrong tagging fraction ω in the equation above. We define thus the experimental distributions

$$\Gamma(B_s\to f)_{\rm exp}=(1-\omega)\Gamma(B_s\to f)+\omega\Gamma(\bar{B}_s\to f),$$
$$\Gamma(\bar{B}_s\to f)_{\rm exp}=(1-\omega)\Gamma(\bar{B}_s\to f)+\omega\Gamma(B_s\to f),$$
$$\Gamma(B_s\to \bar{f})_{\rm exp}=(1-\omega)\Gamma(B_s\to \bar{f})+\omega\Gamma(\bar{B}_s\to \bar{f}),$$
$$\Gamma(\bar{B}_s\to \bar{f})_{\rm exp}=(1-\omega)\Gamma(\bar{B}_s\to \bar{f})+\omega\Gamma(B_s\to \bar{f}).\tag{12}$$

Including the wrong tagging fraction ω, Eqs. (11) can thus be approximated as

$$\Gamma(B_s(t)\to f)=|\langle f|B_s\rangle|^2e^{-\Gamma t}\left\{[1-\omega(1-\rho^2)]\cos^2\frac{\Delta mt}{2}+[\rho^2+\omega(1-\rho^2)]\sin^2\frac{\Delta mt}{2}-(1-2\omega)\rho\sin\phi_{CP}^{+}\sin\Delta mt\right\},$$
$$\Gamma(\overline{B_s}(t)\to f)=|\langle f|B_s\rangle|^2e^{-\Gamma t}\left\{[\rho^2+\omega(1-\rho^2)]\cos^2\frac{\Delta mt}{2}+[1-\omega(1-\rho^2)]\sin^2\frac{\Delta mt}{2}+(1-2\omega)\rho\sin\phi_{CP}^{+}\sin\Delta mt\right\},$$
$$\Gamma(B_s(t)\to \bar{f})=|\langle f|B_s\rangle|^2e^{-\Gamma t}\left\{[\rho^2+\omega(1-\rho^2)]\cos^2\frac{\Delta mt}{2}+[1-\omega(1-\rho^2)]\sin^2\frac{\Delta mt}{2}-(1-2\omega)\rho\sin\phi_{CP}^{-}\sin\Delta mt\right\},$$
$$\Gamma(\overline{B_s}(t)\to \bar{f})=|\langle f|B_s\rangle|^2e^{-\Gamma t}\left\{[1-\omega(1-\rho^2)]\cos^2\frac{\Delta mt}{2}+[\rho^2+\omega(1-\rho^2)]\sin^2\frac{\Delta mt}{2}+(1-2\omega)\rho\sin\phi_{CP}^{-}\sin\Delta mt\right\},\tag{13}$$

One notes that the term including the *CP* violating phase $\phi_{CP}^{\pm}$ vanishes when $\omega=0.5$. It is thus important to develop

a tagging algorithm reducing ω as much as possible. As will be discussed later, for CP eigenstates one has $\rho = 1$ and $\delta_s = 0$. If $\rho = 0$ as for $\bar{B}_s \to D_s^+ \pi^-$, one finds the equations of the sole mixing.

Using all four decays in Eq. (13), one can extract $\sin^2 \phi_{\rm CKM}$ with a twofold ambiguity

$$\sin^2 \phi_{\rm CKM} = \frac{1 + \sin \phi_{CP}^{+} \sin \phi_{CP}^{-} \pm \sqrt{(1 - \sin \phi_{CP}^{+2})(1 - \sin \phi_{CP}^{-2})}}{2}, \tag{14}$$

where $\phi_{\rm CKM} = \pi - \alpha_s + \beta_s = \pi - \gamma + 2\beta_s - \gamma_{ds}$.

B. B_s decays to CP eigenstates

For CP eigenstates one has $\rho = 1$ and $\delta_s = 0$ and one has therefore,

$$\begin{aligned}
&\Gamma(B_s(t) \to f_{CP}) \\
&= |\langle f_{CP}|B_s\rangle|^2 e^{-\Gamma t}\{1 - (1-2\omega)\eta_f \sin\phi_{CP} \sin\Delta m t\}, \\
&\Gamma(\overline{B_s}(t) \to f_{CP}) \\
&= |\langle f_{CP}|B_s\rangle|^2 e^{-\Gamma t}\{1 + (1-2\omega)\eta_f \sin\phi_{CP} \sin\Delta m t\},
\end{aligned} \tag{15}$$

where η_f is the CP eigenvalue of the final state, e.g., $\eta_f = +1$ for $J/\psi\eta$.

C. Strategy to determine the angles β_s and α_s

1. CP eigenstates

Let us now investigate the CP eigenstate final state modes such as $\overline{B_s}(B_s) \to J/\psi\phi$ (for definite longitudinal, parallel or perpendicular transversity polarizations) or $J/\psi\eta$ (see Fig. 5).

The angle β_s can be determined by the angular analysis of $\bar{B}_s(B_s) \to J/\psi\phi \to \mu^+\mu^- K^+ K^-$ [10]. It can also be measured by other decay modes where no angular analysis is necessary, like $\bar{B}_s(B_s) \to J/\psi\eta$.

For a $V_1 - V_2$ final state such as $J/\psi\phi$, η_f depends of the polarization state. For $J/\psi\phi$, it is $\eta_f = +1$ for the longitudinal and parallel polarizations while it is $\eta_f = -1$ for the perpendicular polarization. In case one does not disentangle the polarization by doing a full angular analysis, one would

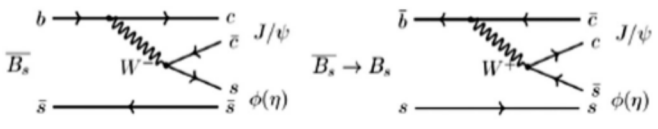

FIG. 5. The leading Feynman diagrams for the $\overline{B_s}$ decay for the final state $J/\psi\phi$ or $J/\psi\eta$. There are also exchange diagrams, which are expected to be small and involve the same CKM elements. Penguin diagrams also exist and include other CKM elements, but they are expected to be negligible.

TABLE I. Polarization fractions of the final state $J/\psi\phi$. It is interesting to note that due to the $V - A$ structure of the SM model, one expects the helicity amplitude $A_+ \simeq 0$, and therefore the relation between transversity fractions $f_\parallel \simeq f_\perp$, in agreement with the measured values within 2σ.

	$f_L = \Gamma_L/\Gamma$	$f_\parallel = \Gamma_\parallel/\Gamma$	$f_\perp = \Gamma_\perp/\Gamma$
CP	$+1$	$+1$	-1
$J/\psi\phi$	0.527 ± 0.008	0.228 ± 0.007	0.245 ± 0.004

have an effective $\eta_f = 1 - 2f_\perp = 0.510 \pm 0.008$ as obtained from the experimentally measured polarizations [7] summarized in Table I.

For this mode one gets the product of the CKM elements,

$$-\frac{V_{tb}^* V_{ts}}{V_{tb} V_{ts}^*} \frac{V_{cb} V_{cs}^*}{V_{cb}^* V_{cs}} = -\frac{V_{tb}^* V_{ts}}{V_{cb}^* V_{cs}} \frac{V_{cb} V_{cs}^*}{V_{tb} V_{ts}^*} = \frac{|V_{cb} V_{cs}^*|^2}{|V_{tb} V_{ts}^*|^2} e^{i(\pi + 2\beta_s)}, \tag{16}$$

and therefore one obtains

$$\phi_{CP}(J/\psi\phi) = \pi + 2\beta_s. \tag{17}$$

From $\bar{B}_s(B_s) \to J/\psi\phi$, LHCb gives the present precision on this angle by the direct measure $\phi_s^{c\bar{c}s} = -2\beta_s = -0.083 \pm 0.041$ [11], compared to the SM model prediction $\beta_s = 0.0185 \pm 0.0003$ [12]. It is worth emphasizing that at present β_s is poorly measured, and that the future experiment at FCC-ee would give a much more precise determination.

2. Non-CP eigenstates

For $\overline{B_s} \to D_s^+ K^-, D^0\phi$, from (8), one gets the invariant product of CKM elements,

$$\begin{aligned}
\lambda(D_s^+ K^-) &= -\frac{V_{tb}^* V_{ts}}{V_{tb} V_{ts}^*} \times \frac{V_{cb} V_{us}^*}{V_{ub}^* V_{cs}} \\
&= \left|\frac{V_{cb} V_{us}^*}{V_{tb} V_{ts}^*}\right| \times \left|\frac{V_{tb}^* V_{ts}}{V_{ub}^* V_{cs}}\right| e^{i\phi_{\rm CKM}},
\end{aligned} \tag{18}$$

where $\phi_{\rm CKM}$ is the weak phase violating CP. One can rewrite the expression above as

$$\begin{aligned}
\lambda(D_s^+ K^-) &= -\frac{V_{tb}^* V_{ts}}{V_{ub}^* V_{cs}} \times \frac{V_{cb} V_{us}^*}{V_{tb} V_{ts}^*} \\
&= \left|\frac{V_{cb}}{V_{ub}}\right|^2 \left|\frac{V_{ub} V_{us}^*}{V_{cb}^* V_{cs}}\right| e^{i(\pi - \alpha_s + \beta_s)},
\end{aligned} \tag{19}$$

and therefore one gets

$$\phi_{\rm CKM}(D_s K) = \pi - (\alpha_s - \beta_s), \tag{20}$$

where α_s and β_s are angles of the second unitarity triangle in Fig. 1. If β_s is known from the angular analysis of

$\bar{B}_s \to J/\psi\phi \to \mu^+\mu^- K^+K^-$, Eq. (20) shows that the modes D_sK would allow a *direct determination* of α_s.

However, with the expected sensitivity at FCC-ee, the determination of the angle β_s in $\bar{B}_s \to J/\psi\phi$ has an important theoretical uncertainty due to penguin diagrams. This uncertainty becomes critical if the ratio of the amplitudes penguin/tree is of $O(3\%)$ or larger. Then, the theoretical error will begin to dominate over the experimental uncertainty.

Since in the SM the sum of the three angles is π, one has $\phi_{\rm CKM} = \pi - (\alpha_s - \beta_s) = 2\beta_s + \gamma_s$, and one could have an estimation of γ_s although this will not be a direct determination since the SM has been assumed. Actually, the sum $\alpha_s + \beta_s + \gamma_s = \pi$ is more general than the SM, as it is a consequence of three-generation unitarity.

This is a similar situation to the angle γ of the ordinary unitarity triangle UT_{db}. It was proposed by I. Dunietz to measure the combination $-(2\beta+\gamma)$ by the decay modes $\bar{B}_d(B_d) \to D^+\pi^-$ and their CP conjugated [13]. The angle β was well known at the time, and this combination could give information on the still poorly determined angle γ.

Therefore, once one obtains a measurement of the angle β_s from CP eigenstates, by using Eq. (20) one could get information on the angle α_s from the time-dependent CP asymmetries for $\overline{B_s} \to D_s^+K^-, D^0\phi$ or $\overline{B_s} \to D_s^-K^+, \bar{D}^0\phi$ and their CP-conjugate modes. On the other hand, since the angle β_s is small, a measurement of $\phi_{\rm CKM}$ (20) would give a rather good preliminary determination of α_s.

Let us now look at relations of $\phi_{\rm CKM}$ to other angles, in particular those of the standard T_{db} triangle. This is possible because the number of independent parameters of the CKM matrix is four, as exposed in Ref. [5].

Indeed, one can write α_s as

$$\begin{aligned}\alpha_s &= \arg\left(-\frac{V_{ub}^*V_{us}}{V_{tb}^*V_{ts}}\right) = \arg\left(-\frac{V_{ub}^*V_{us}}{V_{tb}^*V_{ts}}\times\frac{V_{ud}V_{cb}^*V_{cd}V_{cs}}{V_{ud}V_{cb}^*V_{cd}V_{cs}}\right)\\ &= \arg\left(-\frac{V_{ub}^*V_{ud}}{V_{cb}^*V_{cd}}\right) - \arg\left(-\frac{V_{tb}^*V_{ts}}{V_{cb}^*V_{cs}}\right) + \arg\left(-\frac{V_{cs}^*V_{cd}}{V_{us}^*V_{ud}}\right)\\ &= \gamma - \beta_s + \gamma_{ds}, \end{aligned} \tag{21}$$

where γ is one of the angles of the usual unitarity triangle involving the first and third columns of the CKM matrix and γ_{ds} corresponds to one of the angles of the third triangle in Eq. (2) (see Fig. 1), that is very small. Hence one could approximate α_s by

$$\alpha_s \simeq \gamma - \beta_s, \tag{22}$$

and from relations (20)–(22) one gets, neglecting γ_{ds},

$$\phi_{\rm CKM} \simeq \pi - \gamma + 2\beta_s \tag{23}$$

a relation that would be an interesting test of the CKM scheme, since β_s appears as a correction to an angle of the ordinary unitarity triangle T_{db}.

The determination of γ using $B_s \to D_sK$ was first proposed by R. Aleksan *et al.* [9]. Equation (23) is known [14], and has been proposed at LHCb to measure the angle γ once β_s would be measured from the angular analysis of time-dependent CP violation in $\bar{B}_s(B_s) \to J/\psi\phi \to \mu^+\mu^-K^+K^-$.

III. EXPERIMENTAL EXPECTATIONS AT FCC-ee

As one can see in Eqs. (13) and (15), CP violating effects are damped by the fraction of wrong tagging ω. Table II shows typical tagging performances of some experiments. It is thus essential to measure this factor precisely. Fortunately, the decay $\overline{B_s} \to D_s^+\pi^-$ allows one to measure the value of ω very precisely.

A. Generic detector resolutions

In order to carry out experimental studies, we define a generic detector, the resolution of which is parametrized as follows:

Acceptance	$\lvert\cos\theta\rvert$	$<$	0.95
Charged particles			
p_T resolution	$\frac{\sigma(p_T)}{p_T^2}$	$=$	$2.\times10^{-5} \oplus \frac{1.2\times10^{-3}}{p_T\sin\theta}$
ϕ,θ resolution	$\sigma(\phi,\theta)\mu$rad	$=$	$18 \oplus \frac{1.5\times10^{3}}{p_T\sqrt{\sin\theta}}$
Vertex resolution	$\sigma(d_{\rm Im})\mu$m	$=$	$1.8 \oplus \frac{5.4\times10^{1}}{p_T\sqrt{\sin\theta}}$
e,γ particles			
Energy resolution	$\frac{\sigma(E)}{E}$	$=$	$\frac{5\times10^{-2}}{\sqrt{E}} \oplus 5\times10^{-3}$
EM ϕ,θ resolution	$\sigma(\phi,\theta)$ mrad	$=$	$\frac{7}{\sqrt{E}}$

(24)

where θ, ϕ are the particles' polar and azimuthal angles respectively, p_T (in GeV) the track transverse momentum, E the $e^\pm, \gamma$ energy and $d_{\rm Im}$ the tracks' impact parameter.

B. Measuring the wrong tagging fraction

In order to extract experimentally the CKM phases using the time-dependent distributions in Eqs. (13) and (15), one needs to measure precisely the wrong tagging fraction. This can be done by using the decay $\overline{B_s} \to D_s^+\pi^- \to (\phi\pi^+)_{D_s}\pi^- \to K^+K^-\pi^+\pi^-$. Indeed, only one diagram is involved in this decay (see Fig. 6) and thus no CP violation is expected. Furthermore its branching fraction is relatively large ($\sim 3\times10^{-3}$). Some 13.8×10^6 $B_s + \overline{B_s}$ such decays are

TABLE II. Typical tagging figure of merit for some experiments, where ϵ is the tagging efficiency and ω the wrong tagging fraction, in the range 0–0.5.

Tagging merit	LEP	*BABAR*	LHCb
$\epsilon(1-2\omega)^2$	25–30%	30%	6%

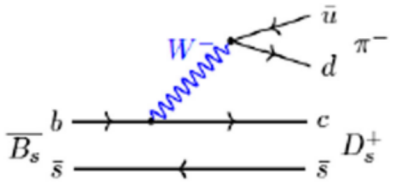

FIG. 6. The Feynman diagrams for the $\overline{B_s}$ decay for the final state $D_s^+\pi^-$. This decay involves only one diagram, hence is very convenient for probing the B_s tagging.

expected to be produced at FCC-ee when accumulating 150 ab^{-1} at the Z-pole (see Table III). One gets the time-dependent distributions from Eq. (13) with $\rho = 0$.

$$\Gamma(B_s(t) \to D_s^-\pi^+) = |\langle D_s^-\pi^+|B_s\rangle|^2 e^{-\Gamma t}\left\{(1-\omega)\cos^2\frac{\Delta mt}{2} + \omega\sin^2\frac{\Delta mt}{2}\right\},$$

$$\Gamma(\overline{B_s}(t) \to D_s^-\pi^+) = |\langle D_s^-\pi^+|B_s\rangle|^2 e^{-\Gamma t}\left\{\omega\cos^2\frac{\Delta mt}{2} + (1-\omega)\sin^2\frac{\Delta mt}{2}\right\},$$

$$\Gamma(B_s(t) \to D_s^+\pi^-) = |\langle D_s^-\pi^+|B_s\rangle|^2 e^{-\Gamma t}\left\{\omega\cos^2\frac{\Delta mt}{2} + (1-\omega)\sin^2\frac{\Delta mt}{2}\right\},$$

$$\Gamma(\overline{B_s}(t) \to D_s^+\pi^-) = |\langle D_s^-\pi^+|B_s\rangle|^2 e^{-\Gamma t}\left\{(1-\omega)\cos^2\frac{\Delta mt}{2} + \omega\sin^2\frac{\Delta mt}{2}\right\}, \quad (25)$$

TABLE III. The expected number of produced $\overline{B_s}$ decays to specific decay modes at FCC-ee at a center of mass energy of 91 GeV over five years with two detectors. These numbers have to be multiplied by two when including B_s decays. The branching fractions of the Particle Data Group [7] have been used.

$E_{cm} = 91.2$ GeV and $\int L = 150$ ab^{-1}			
$\sigma(e^+e^- \to Z)$ nb	Number of Z	$f(Z \to \overline{B_s})$	Number of produced $\overline{B_s}$
~42.9	~6.4 10^{12}	0.0159	~1 10^{11}
$\overline{B_s}$ decay mode	Decay mode	Final state	Number of $\overline{B_s}$ decays
		CP eigenstates	
$D_s^+\pi^-$	$D_s^+ \to \phi\pi$	$K^+K^-\pi^+\pi^-$	~6.9 10^6
$D_s^+\pi^-$	$D_s^+ \to \phi\rho$	$K^+K^-\pi^+\pi^-\pi^0$	~12.9 10^6
$D_s^+K^-$	$D_s^+ \to \phi\pi$	$K^+K^-\pi^+K^-$	~5.2 10^5
$D_s^+K^-$	$D_s^+ \to \phi\rho$	$K^+K^-\pi^+K^-\pi^0$	~9.8 10^5
$D^0\phi$	$D^0 \to K\pi$	$K^-\pi^+K^+K^-$	~6.1 10^4
$D^0\phi$	$D^0 \to K\rho$	$K^-\pi^+K^+K^-\pi^0$	~1.7 10^5
		CP eigenstates	
$J/\psi\phi$	$J/\psi \to \mu^+\mu^-$	$\mu^+\mu^-K^+K^-$	~3.2 10^6
$J/\psi\eta$	$J/\psi \to \mu^+\mu^-$	$\mu^+\mu^-\gamma\gamma$	~9.6 10^5

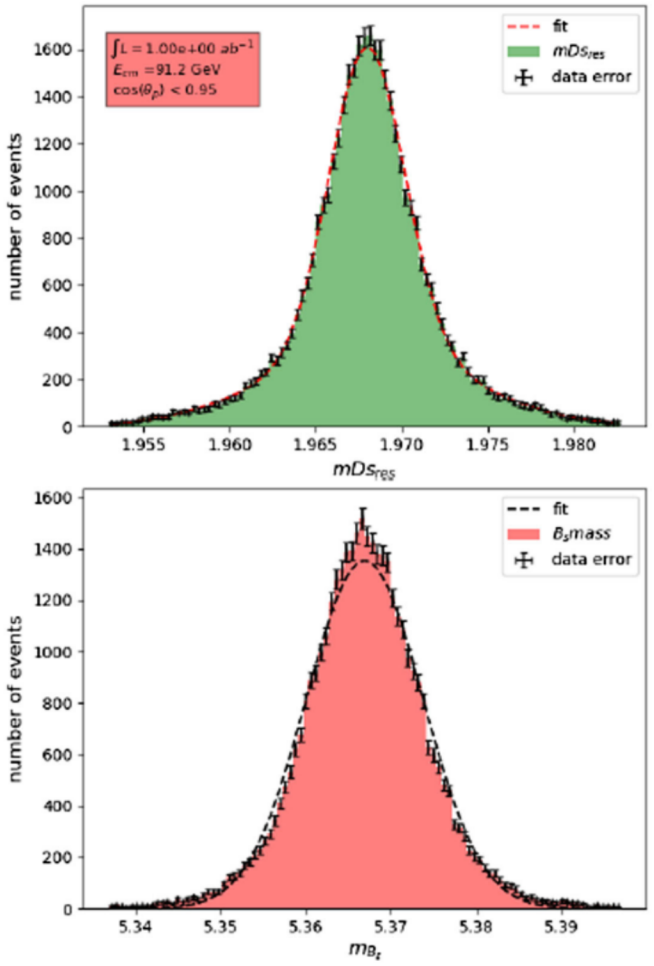

FIG. 7. D_s (upper plot) and B_s (lower plot) mass resolutions in $e^+e^- \to Z \to \overline{B_s}(B_s) \to D_s^\pm\pi^\mp \to K^+K^-\pi^+\pi^-$. One obtains $\sigma(m_{D_s}) \simeq 3.2$ MeV and $\sigma(m_{B_s}) = 6.7$ MeV. The geometric acceptance of the detector ($|\cos\theta| < .95$) leads to an efficiency of 86% for this four-body final state.

The main source of background is the combinatorial one, which is however expected to be small, thanks to the excellent mass resolution on D_s and B_s as shown in Fig. 7.

The expected time-dependent distributions corresponding to the Eqs. (25) are shown in Fig. 8. One extracts the resolution of the wrong tagging parameter ω by fitting these time-dependent distributions. Thanks to the large statistics available, one finds $\sigma(\omega) \simeq 1.4 \times 10^{-4}$. The oscillation frequency $\Delta m/\Gamma$ is also obtained with a resolution of about 5×10^{-4}. In these figures, no resolution on the flight distance has been included.

There are three sources of smearing of the B_s oscillation frequency.

(1) The uncertainty on the B_s reconstructed momentum: In Fig. 9 (upper plot) we show the B_s flight distance. The average distance is ~2.8 mm. In Fig. 9 (lower plot) we show the resolution on flight

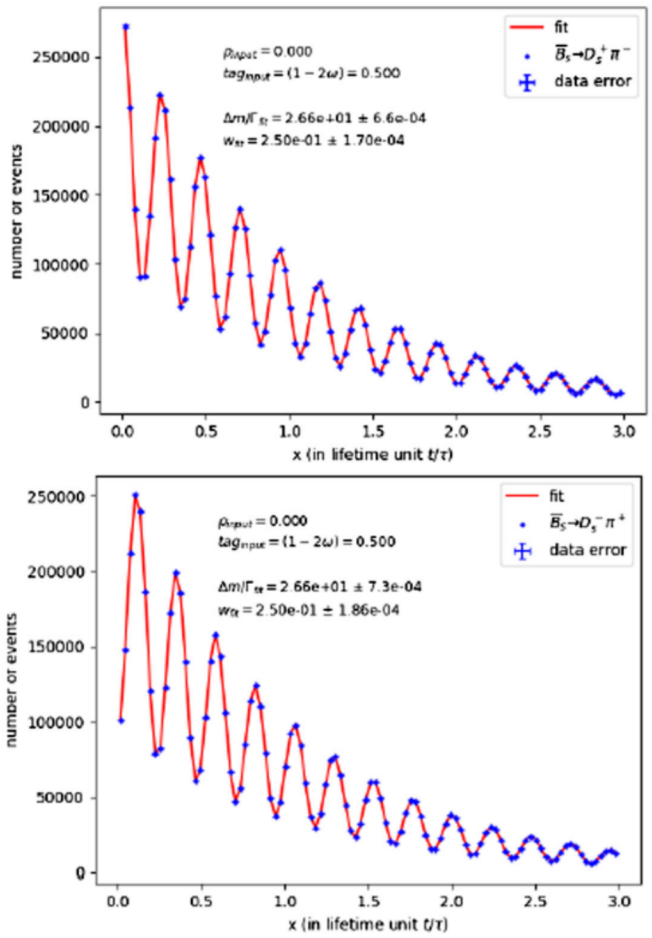

FIG. 8. The time-dependent distribution for $B_s \to D_s^- \pi^+ + CP$ conjugate (upper plot) and $B_s \to D_s^+ \pi^- + CP$ conjugate (lower plot). The overall statistical resolution on ω is 1.4×10^{-4}.

distance due to the error on B_s reconstructed momentum, which is negligible.

(2) The uncertainty on primary vertex position: This resolution is obtained by a combination of the beam interaction point (IP) and reconstructed primary vertex. The error on the IP position at FCC-ee is obtained from the beam size; $\sigma(\mathrm{IP}_x) \simeq 4.5\ \mu\mathrm{m}$, $\sigma(\mathrm{IP}_y) \simeq 0.02\ \mu\mathrm{m}$ and $\sigma(\mathrm{IP}_z) \simeq 0.30$ mm. Combining these constraints with the measured tracks originating from the primary vertex results in an overall negligible primary vertex resolution.

(3) The uncertainty on B_s decay vertex position: This has been evaluated to be the dominant contribution. However, it is estimated that its impact on the B_s flight distance is of the order of $\sim 18\ \mu$m (see Appendix). Overall, the resolution on the B_s flight distance remains below 20 μm, and thus leads to a minor damping of the time dependent curves, which does not significantly affect the measurement of the *CP* violating angles.

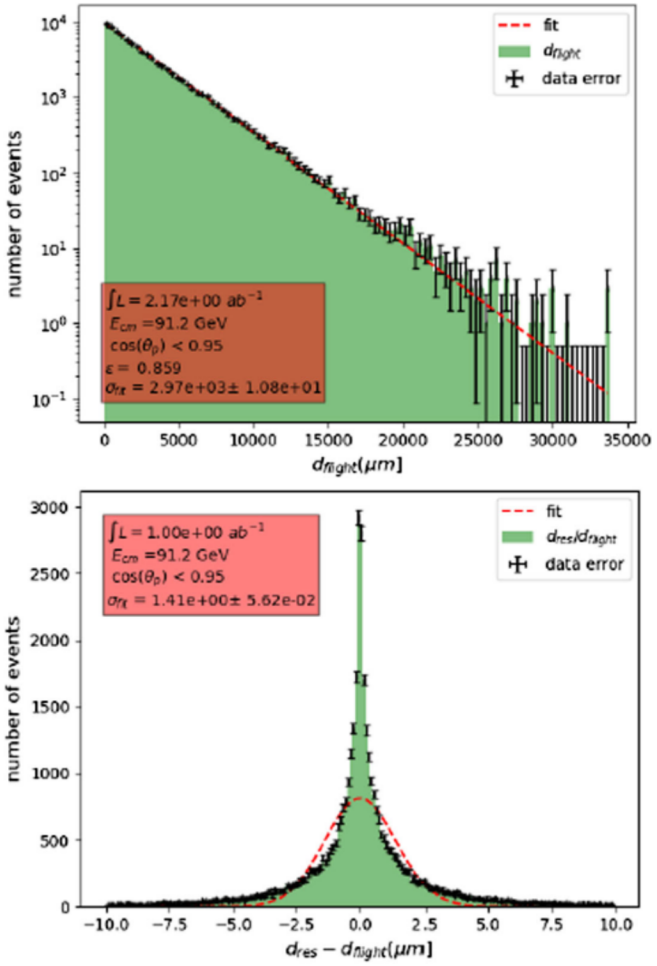

FIG. 9. B_s decay distance (upper plot) and resolution on decay distance due to momentum resolution (lower plot) in $e^+e^- \to Z \to \overline{B_s}(B_s) \to D_s^{\pm}\pi^{\mp} \to K^+K^-\pi^+\pi^-$. The uncertainty is 1.4 μm, and is negligible compared to the average flight distance of 3 mm.

C. Measurement of the CKM angles α_s and β_s

We have now all the ingredients to evaluate the sensitivity on the CKM angles α_s and β_s with the decays $\overline{B_s}(B_s) \to D_s^{\pm}K^{\mp}$ and $\overline{B_s}(B_s) \to J/\psi\phi$, respectively, which one expects at FCC-ee.

Let us first concentrate on $\overline{B_s}(B_s) \to D_s^{\pm}K^{\mp}$. We simulate these reactions with the parametrized detector using some specific values for the strong phase difference, $\delta_s = 40°$, and the CKM phase, $\phi = 70°$, which is very close to the expected value from the present indirect constraints on the angles of the corresponding unitarity triangle. We show in Fig. 10 the signal together with the main sources of background, with the expectation of the combinatorial one, which is however expected to be small, thanks to the excellent mass resolution.

As can be seen in Fig. 10, the signal is already rather clean without PID but becomes very clean once a simple PID is turned on. Using the signal, the time-dependent

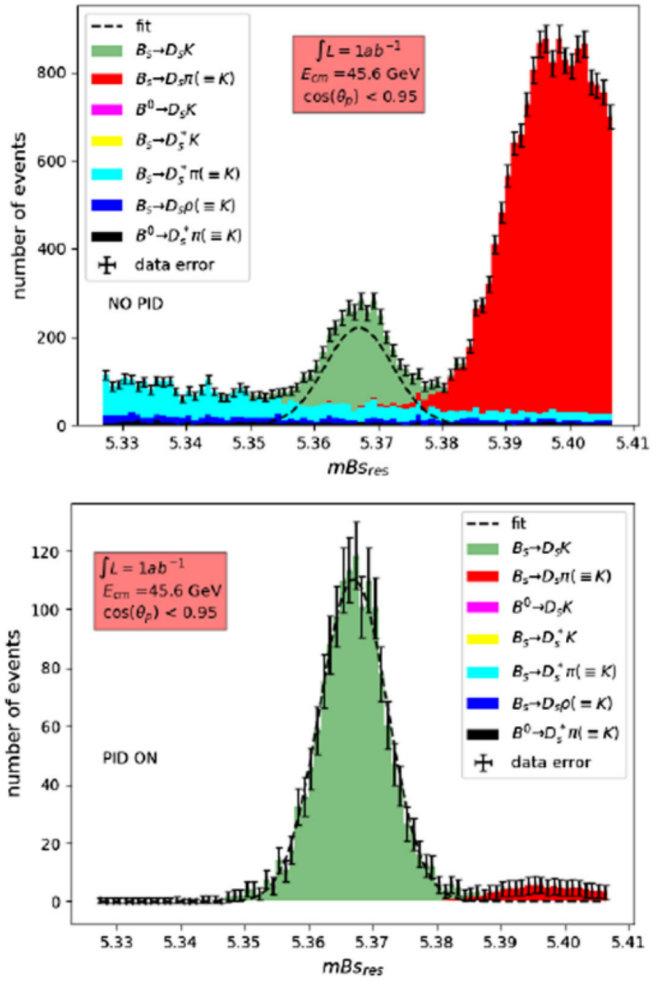

FIG. 10. B_s mass resolutions in $\overline{B_s}(B_s) \to D_s^{\pm} K^{\mp}$ decays in $e^+e^- \to Z \to \overline{B_s}(B_s) \to D_s^{\pm} K^{\mp} \to \phi\pi^{\pm} K^{\mp} \to K^+K^-\pi^{\pm}K^{\mp}$. The upper histogram shows the signal and backgrounds without particle identification. A simple particle identification (PID) based on time of flight and dE/dx is turned on for the lower histogram.

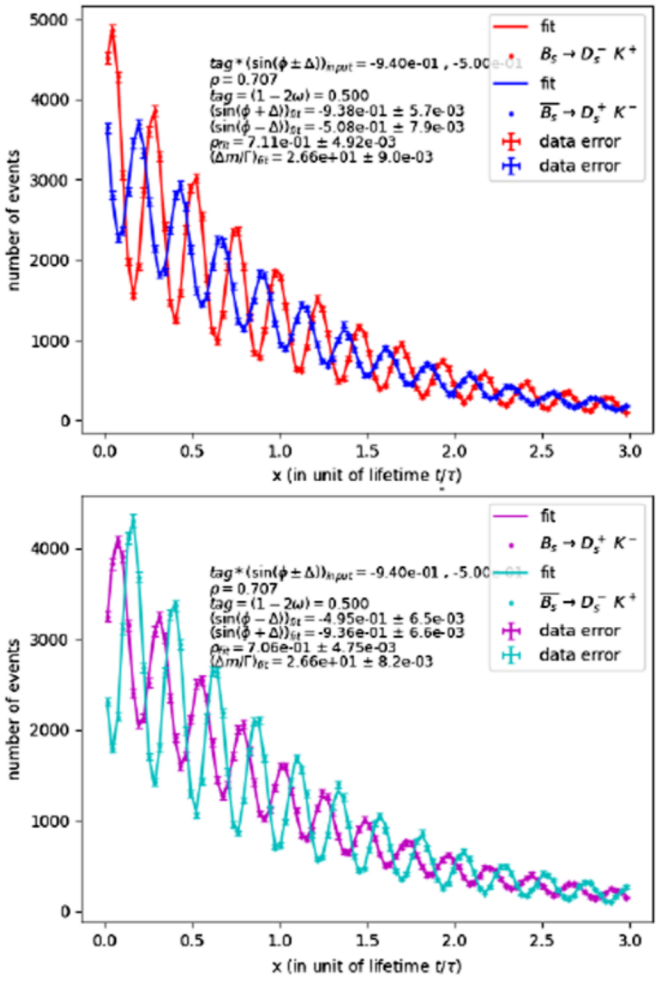

FIG. 11. $\overline{B_s}(B_s) \to D_s^{\pm} K^{\mp}$ time-dependent distributions (upper and lower plots) with the statistics of 150 ab^{-1} expected at FCC-ee.

distributions corresponding to Eqs. (13) are shown in Fig. 11. From a global fit of these four time-dependent distributions, one extracts the resolution on the CKM phase Φ and the strong phase difference δ_s. Thanks to the large statistics available, one finds $\sigma(\Phi) \simeq 0.4°$.

Note that this resolution could be further improved by using several other B_s final states involving the same CKM phase, such as $D_s^{*\pm} K^{\mp}$ or $D_s^{\pm} K^{*\mp}$. In addition one can use other D_s final states, such as $D_s^{\pm} \to \overline{K^{*0}}(K^{*0}) K^{\pm} \to K^+K^-\pi^{\pm}$ and $D_s^{\pm} \to \phi\rho^{\pm} \to K^+K^-\pi^{\pm}\pi^0$. However, since several of these modes include neutral particles, excellent electromagnetic calorimeter resolutions are crucial to reject the backgrounds.

We now focus on $\overline{B_s}(B_s) \to J/\psi\phi$ decaying to the four-body final state $\mu^+\mu^-K^+K^-$. The geometric acceptance is very similar to $D_s^{\pm}\pi^{\mp} \to K^+K^-\pi^+\pi^-$. The B_s mass resolution is also very similar to $D_s^{\pm}\pi^{\mp}$. We show in Fig. 12 the J/ψ mass resolution. From the time-dependent fit (Fig. 12), $\sin\phi = \sin 2\beta_s$ is measured. Thanks to the very hight statistics this lead to the resolution $\sigma(\beta_s) = 0.035°$, while this angle is expected to be $\sim 1°$. This sensitivity assumes that a full angular analysis is carried out since this two-vector final state includes $CP = +1$ and $CP = -1$ contributions. If one does a simple time-dependent analysis as in Fig. 12, the amplitude of the interference is reduced by factor $1 - 2f_{\perp} \simeq 0.5$, as already mentioned. This leads to $\sigma(\beta_s) = 0.07°$. Interestingly, the impact of the present error on $f_{\perp}$ is negligible. Part of this reduced sensitivity can be mitigated by using additional J/ψ final states such as $e^+e^-(\gamma)$ or other modes, such as $J/\psi\eta$, which is a pure $CP = +1$ eigenstate and does not necessitate an angular analysis. In this latter mode, an excellent electromagnetic calorimeter is required to reject the backgrounds. In summary, the resolution of $\sigma(\beta_s) = 0.035°$ mentioned above, is reachable.

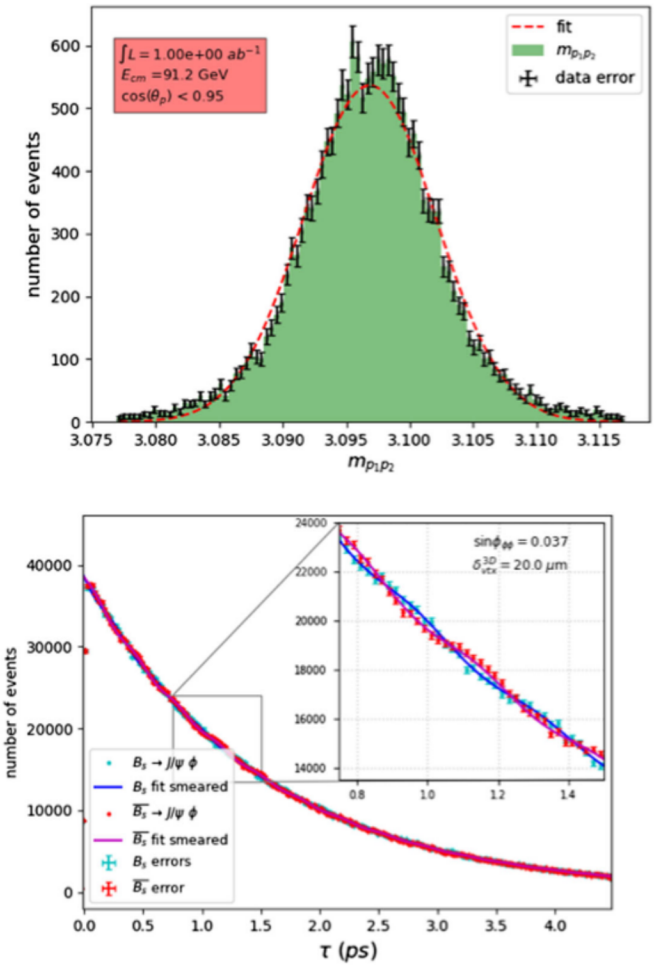

FIG. 12. $\overline{B_s}(B_s) \to J/\psi\phi$ decay in $e^+e^- \to Z \to \overline{B_s}(B_s) \to J/\psi\phi \to \mu^+\mu^- K^+K^-$. The upper plot shows the reconstructed J/ψ mass. A resolution of ~5.2 MeV is observed. The two time-dependent distributions [Eq. (15)] are shown in the lower plot with the statistics of 150 ab^{-1} expected at FCC-ee.

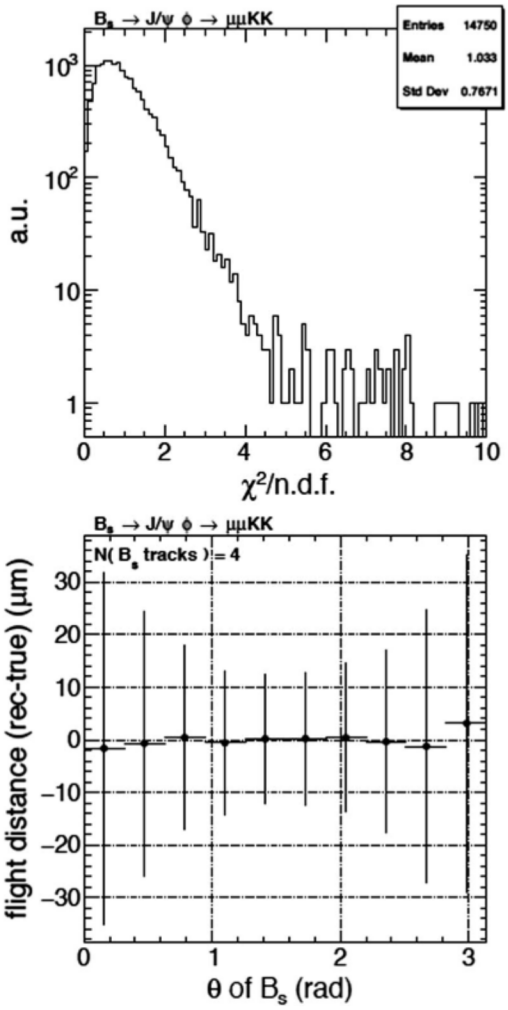

FIG. 13. Upper plot: Distribution of the normalised χ^2 of the fit of the $B_s \to J/\psi\phi \to \mu\mu KK$ vertex. Lower plot: Profile histogram of the difference between the reconstructed and the generated B_s flight distance, as a function of the B_s polar angle, for the $B_s \to J/\psi\phi \to \mu\mu KK$ decay. The error bars show the rms of the distribution in each bin, hence the resolution in the flight distance.

IV. CONCLUSIONS

In summary, we have shown that excellent resolutions on the angles α_s and β_s are expected at FCC-ee with $\sigma(\alpha_s) \simeq 0.4°$ and $\sigma(\beta_s) \simeq 0.035°$. These angles are two angles of the unitarity triangle UT_{sb} defined in Eq. (2) and Fig. 1. The angle directly measured by the mode $\overline{B_s}(B_s) \to D_s^{\pm}K^{\mp}$ is given by (20) $\phi_{D_sK} = \pi - (\alpha_s - \beta_s)$ and the mode $\overline{B_s}(B_s) \to J/\psi\phi$ gives a direct measurement of the angle (17) $\phi_{J/\psi\phi} = \pi + 2\beta_s$. In a forthcoming paper [8] it is shown that the modes $B^{\pm} \to \bar{D}^0(D^0)K^{\pm} \to K^+K^-K^{\pm}$ and $B^{\pm} \to \bar{D}^0(D^0)K^{\pm} \to K_s\pi^0K^{\pm}$ enable one to measure directly $\phi_{D^0K} = \pi + \gamma_s$. Interestingly, should unitarity hold, one has a simple relation between these observable phases, $-\phi_{D_sK} + \phi_{J/\psi\phi} + \phi_{D^0K} = 0(\text{ mod } 2\pi)$. All the angles of the flat unitarity triangle UT_{sb} can thus be determined directly with high accuracy.

APPENDIX: RESOLUTIONS IN THE RECONSTRUCTED FLIGHT DISTANCES

The resolutions in the reconstructed B_s flight distances have been determined using Monte-Carlo events that were passed through a fast simulation of the tracking system of the experiment based on DELPHES [15]. The PYTHIA8 Monte-Carlo generator was used to simulate the production of $b\bar{b}$ pairs and the decays of the B_s mesons were performed with the EvtGen program. The resulting charged particles were turned into simulated tracks using the "TrackCovariance" fast tracking software implemented in DELPHES. It relies on a description of the tracker geometry. The vertex detector and the drift chamber of the IDEA detector [3], which provide resolutions similar to the ones given in Sec. III.1, are used here. In this geometry, the

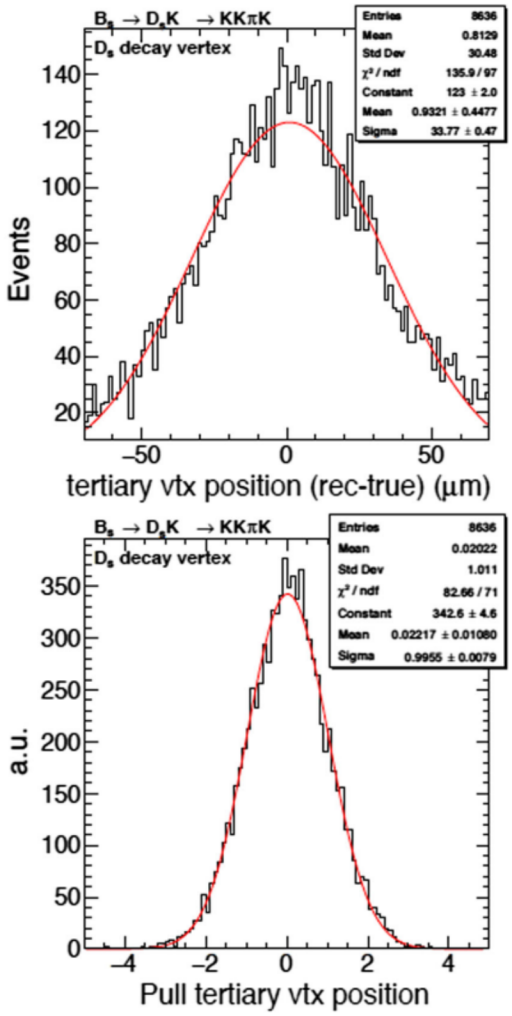

FIG. 14. Upper plot: Resolution in the reconstructed position of the D_s decay vertex in the decay $B_s \to D_sK \to KK\pi K$. Lower plot: pull of this reconstructed position. The red curves show the results of a Gaussian fit to the histograms.

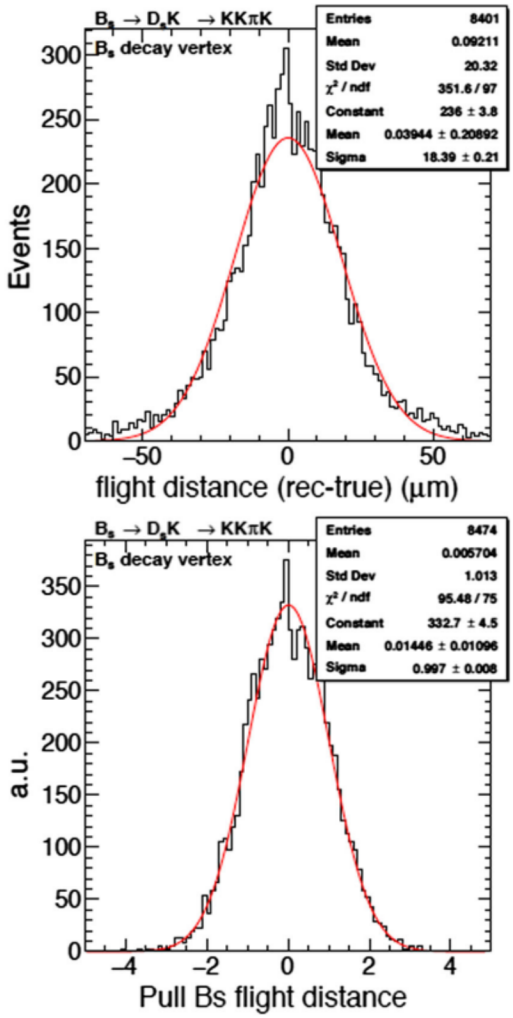

FIG. 15. Upper plot: Resolution in the reconstructed flight distance of the B_s in the decay $B_s \to D_sK \to KK\pi K$. Lower plot: pull of this flight distance. The red curves show the results of a Gaussian fit to the histograms.

central beampipe has an inner radius of 1.5 cm and the innermost layer of the vertex detector is at 1.7 cm of the beampipe center. The tracking software accounts for the finite detector resolution and for the multiple scattering in each tracker layer and determines the (nondiagonal) covariance matrix of the helix parameters that describe the trajectory of each charged particle. This matrix is then used to produce a smeared five-parameter track, for each charged particle emitted within the angular acceptance of the tracker.

A simple standalone code is used to fit a given set of tracks to a common vertex [16], under the assumption that the trajectories be perfect helixes. When reconstructing the vertex corresponding to a given decay, a perfect "seeding" is assumed. For example, for the decay $B_s \to J/\psi\phi \to \mu\mu KK$, the vertex is reconstructed using the simulated tracks created from the muons and kaons that correspond to this decay. Once the B_s decay vertex is reconstructed, the flight distance of the B_s is taken to be the distance of this vertex to the nominal interaction point.[1] The distribution of the difference between the reconstructed flight distance and the flight distance given by the Monte-Carlo information is approximately Gaussian, and its rms can be used to define the resolution in the reconstructed flight distance. This resolution is shown in Fig. 13 as a function of the polar angle of the B_s, for the $B_s \to J/\psi\phi \to \mu\mu KK$ decay. As expected, better resolutions are obtained in the central region, since the tracks suffer less multiple scattering than in the forward region. The figure also shows the

[1]No attempt is made here to reconstruct the primary vertex of the event. However, it was checked that with a beam-spot constraint, the primary vertex can be reconstructed with a resolution of $4\mu m$–$5\mu m$ in $b\bar{b}$ events, leading to a negligible contribution to the resolution in the B_s flight distance.

distribution of the normalized χ^2 of the vertex fit, whose average is at one, as expected.

The reconstruction of the B_s decay vertex in $B_s \to D_s K$ is more complicated since D_s does not decay promptly but leads to a tertiary vertex. In a first step, the $D_s \to KK\pi$ decay vertex is reconstructed, using the tracks corresponding to the three daughter particles of the D_s. When three tracks are reconstructed (about 95% of the events), the position of the D_s vertex (the $3D$ distance between the vertex and the origin) is reconstructed with a resolution of about 33 μm, as shown in the upper panel of Fig. 14. The lower panel in the same figure illustrates the good quality of the fit; from the covariance matrix of the coordinates of the D_s vertex, an uncertainty on the D_s vertex position is computed, and is used to determine the corresponding pull, i.e., the difference between the reconstructed and the generated D_s vertex positions divided by this uncertainty. As expected, the distribution of the pull is gaussian with a variance of unity. The momenta of the tracks corresponding to the D_s daughters are then propagated to the D_s decay vertex, such that their sum gives the three-momentum of the D_s when it decays. From the D_s momentum at its decay point and the coordinates of this decay vertex, a D_s "pseudotrack" can be reconstructed, i.e., a set of five parameters that describe the D_s helicoidal trajectory. In order to use this pseudotrack in the vertex fitter together with the track associated with the "bachelor" kaon (the K from the $B_s \to D_s K$ decay) to reconstruct the B_s decay vertex, the covariance matrix of the D_s pseudo-track must be determined. This is done using a bootstrap method:

(a) the parameters of the D_s daughters' tracks are smeared according to their covariance matrices;
(b) a D_s vertex is refit using these smeared tracks, which are propagated to this vertex to define a D_s momentum, and the five parameters of a D_s pseudotrack;
(c) the covariance matrix of the D_s track parameters is obtained by statistical inference, over a large sample of D_s pseudotracks obtained from smearing the D_s daughter tracks many times.

Figure 15 shows that, from the D_s pseudotrack and the track of the bachelor K, the vertex fitter reconstructs the B_s decay vertex with a resolution of about 18 μm, and that the pull of this B_s flight distance is distributed as expected.

[1] M. Bicer *et al.*, J. High Energy Phys. 01 (2014) 164.
[2] A. Abada *et al.* (FCC Collaboration), Eur. Phys. J. C **79**, 474 (2019).
[3] A. Abada *et al.* (FCC Collaboration), Eur. Phys. J. Special Topics **228**, 261 (2019).
[4] M. Kobayashi and T. Maskawa, Prog. Theor. Phys. **49**, 652 (1973).
[5] R. Aleksan, B. Kayser, and D. London, Phys. Rev. Lett. **73**, 18 (1994).
[6] I. Dunietz, R. Fleischer, and U. Nierste, Phys. Rev. D **63**, 114015 (2001); A. Lenz and U. Nierste, J. High Energy Phys. 06 (2007) 072.
[7] P. A. Zyla *et al.* (Particle Data Group), Prog. Theor. Exp. Phys. (**2020**), 083C01.
[8] R. Aleksan, L. Oliver, and E. Perez, arXiv:2107.02002.
[9] R. Aleksan, I Dunietz, and B. Kayser, Z. Phys. C **54**, 653 (1992).
[10] A. Dighe, I. Dunietz, and R. Fleischer, Eur. Phys. J. C **6**, 647 (1999).
[11] R. Aaij *et al.* (LHCb Collaboration), Eur. Phys. J. C **79**, 706 (2019); **80**, 601(E) (2020).
[12] S. Descotes-Genon and P. Koppenburg, Annu. Rev. Nucl. Part. Sci. **67**, 97 (2017).
[13] I. Dunietz, Phys. Lett. B **427**, 179 (1998).
[14] J. Nardulli, arXiv:0807.1670.
[15] J. de Favereau, C. Delaere, P. Demin, A. Giammanco, V. Lemaître, A. Mertens *et al.*, J. High Energy Phys. (2014).
[16] F. Bedeschi (private communication).